Automatic detection of small-scale EUV brightenings observed by the Solar Orbiter/EUI

N. Alipour[1], H. Safari[1,2,⋆], C. Verbeeck[3], D. Berghmans[3], F. Auchère[4], L. P. Chitta[5], P. Antolin[6], K. Barczynski[7,8], É. Buchlin[4], R. Aznar Cuadrado[5], L. Dolla[3], M. K. Georgoulis[9], S. Gissot[3], L. Harra[8,7], A. C. Katsiyannis[3], D. M. Long[10], S. Mandal[5], S. Parenti[4], O. Podladchikova[11], E. Petrova[12], É. Soubrié[4], U. Schühle[5], C. Schwanitz[8], L. Teriaca[5], M. J. West[13], and A. N. Zhukov[3,14]

(Affiliations can be found after the references)

ABSTRACT

Context. Accurate detections of frequent small-scale extreme ultraviolet (EUV) brightenings are essential to the investigation of the physical processes heating the corona.
Aims. We detected small-scale brightenings, termed campfires, using their morphological and intensity structures as observed in coronal EUV imaging observations for statistical analysis.
Methods. We applied a method based on Zernike moments and a support vector machine (SVM) classifier to automatically identify and track campfires observed by Solar Orbiter/Extreme Ultraviolet Imager (EUI) and Solar Dynamics Observatory (SDO)/Atmospheric Imaging Assembly (AIA).
Results. This method detected 8678 campfires (with length scales between 400 km and 4000 km) from a sequence of 50 High Resolution EUV telescope (HRI$_{EUV}$) 174 Å images. From 21 near co-temporal AIA images covering the same field of view as EUI, we found 1131 campfires, 58% of which were also detected in HRI$_{EUV}$ images. In contrast, about 16% of campfires recognized in HRI$_{EUV}$ were detected by AIA. We obtain a campfire birthrate of $2 \times 10^{-16} \mathrm{m}^{-2} \mathrm{s}^{-1}$. About 40% of campfires show a duration longer than 5 s, having been observed in at least two HRI$_{EUV}$ images. We find that 27% of campfires were found in coronal bright points and the remaining 73% have occurred out of coronal bright points. We detected 23 EUI campfires with a duration greater than 245 s. We found that about 80% of campfires are formed at supergranular boundaries, and the features with the highest total intensities are generated at network junctions and intense H I Lyman-α emission regions observed by EUI/HRI$_{Lya}$. The probability distribution functions for the total intensity, peak intensity, and projected area of campfires follow a power law behavior with absolute indices between 2 and 3. This self-similar behavior is a possible signature of self-organization, or even self-organized criticality, in the campfire formation process.

Key words. Sun: corona – Sun: UV radiation – Techniques: high angular resolution

1. Introduction

Brightenings in the extreme ultraviolet (EUV) have been observed in the solar atmosphere for many years (Vaiana et al. 1973a,b; Golub et al. 1974; Alipour & Safari 2015; Madjarska 2019; Shokri et al. 2022). The smallest of these brightenings in the quiet Sun (QS) were measured by Berghmans et al. (2021) in 174 Å images taken by the Extreme Ultraviolet Imager (EUI, Rochus et al. 2020) on board the Solar Orbiter mission (Müller et al. 2020). These tiny EUV brightenings, coined "campfires" in the quiet Sun that have been found to date are short-lived events in the low corona with structures that take the form of small-scale loops, elongated loops, loop apexes, and contact points between loops (Berghmans et al. 2021; Mandal et al. 2021). These campfires have length scales ranging from 400 to 4000 km with typical lifetimes of less than 200 s. Campfires reach temperatures peaking at about 1 MK (Berghmans et al. 2021) and occur at heights of 1 to 5 Mm above the Sun's visible surface (Zhukov et al. 2021).

Campfires may be rooted in low-lying magnetic structures, and magnetic reconnection might be their formation mechanism, however this has not yet been shown beyond reasonable doubt. Hence, one aspect to explore is to check for similarities

to other flaring events, for instance, large flares, microflares, and nanoflares (Parker 1988). Panesar et al. (2021) studied the magnetic properties of 52 campfires and found that most of them occur above magnetic polarity inversion (i.e., "neutral") lines with a magnetic flux cancelation rate of 10^{18} Mx hr^{-1}. These authors concluded that magnetic flux cancelation could be the primary mechanism in the formation of campfires. Also, they estimated the magnetic energy for the system of campfires in the range 10^{26} to 10^{27} erg, which might be sufficient to locally heat the solar corona depending on their occurrence frequency. Chen et al. (2021) used a 3D magnetohydrodynamic simulation with MURaM code and came to the conclusion that magnetic reconnection may well be the primary driver of most campfires. They also proposed that campfires can significantly contribute to quiet-Sun coronal heating.

Chitta et al. (2021) recently applied an automatic method based on different intensity thresholds to Atmospheric Imaging Assembly (AIA) images to identify such tiny flare-like phenomena. These authors estimated about 100 small events emerge per second on the entire Sun, which is insufficient to supply the required energy for quiet Sun coronal heating. Coronal bright points (CBPs) are larger brightenings that include small-scale loops in the low corona with X-ray or EUV emissions (Madjarska 2019). Alipour & Safari (2015) studied the

statistical properties of the CBPs in EUV emissions observed by AIA during 4.4 years. They calculated an average size of 130 Mm^2 and a lifetime ranging from a few minutes to several days. Hosseini Rad et al. (2021) calculated the energy loss of CBPs. They also showed that by extending the CBPs' energy to nanoflares ($> 10^{24}$ erg), the contribution of small-scale bursts might increase significantly, along with their importance for heating the corona.

Due to the variety in morphology, structure, and intensity of campfires, along with their large numbers, automatic detection methods need to be developed to identify, track, and determine the occurrence frequency of these events that may play a role in coronal heating. We applied an automatic detection algorithm for campfires by analyzing various properties. In particular, we used the Zernike moments (ZMs; Khotanzad & Hong 1990) and the support vector machine (SVM; Hsu et al. 2011) to identify campfires from both HRI$_{EUV}$ at 174 Å and AIA at 171 Å observations. The first few low-order ZMs describe the centroid of an image and its orientation; however, higher order ZMs provide information about geometry and structures (lines, shapes, etc.) of the objects Alipour et al. (2019). Since ZMs define mapping an image to the orthogonal complete set of functions (Zernike polynomials), the correspondent moments are unique and independent features. Therefore, these particular properties for ZMs demonstrate that ZMs are suitable for training a classification machine. A sub-image with various sizes may contain a campfire or not, thus, the SVM as a mainly double-class classifier is applied to recognize campfire and non-campfire sub-images.

This work is organized as follows: Section 2 gives an overview of data analysis. The automatic identification and tracking algorithms are explained in Section 3. The statistical analysis and results are presented in Section 4. Finally, the work is summarized and concluded in Section 5.

2. Data

The EUI is an instrument onboard the Solar Orbiter mission (Müller et al. 2020) with a Full-Sun Imager (FSI) and two High-Resolution Imager (HRI) telescopes (Rochus et al. 2020). The HRI$_{EUV}$ telescope samples at 174 Å and is sensitive to temperatures of 1 MK. The HRI$_{Lya}$ telescope observes images in the hydrogen Lyman-α passband centered at 1216 Å. To study the statistical properties of campfires, we used the sequence of 50 HRI$_{EUV}$ and HRI$_{Lya}$ images[1] with a cadence of 5 s during a 245 s time interval from 30 May 2020. On 30 May 2020, the HRI$_{EUV}$ FOV covered the SDO line-of-sight regions (Berghmans et al. 2021, Figure 1 therein). During these observations, Solar Orbiter was located at a distance of 0.556 AU from the Sun, which resulted in a pixel size of 198 km. To compare the AIA (Lemen et al. 2012) and HRI$_{EUV}$ images, we correct for the difference in light travel time of 220 s for the two spacecrafts. We analyzed 21 AIA images at 171 Å during the same observation period. Figure 1 represents the observation time interval for HRI$_{EUV}$ (blue lines), AIA (red lines), and simultaneously EUI and AIA (black lines) from the first simultaneous (EUI and AIA) image at 2020-05-30 14:54:05 UT. The last simultaneous (EUI and AIA) image was observed at 2020-05-30 14:58:05 UT. We analysed the AIA observations to compare the campfires detected in both instruments. To do this, we re-mapped all images to the Carrington coordinate system. Following Berghmans et al. (2021), to preserve the HRI$_{EUV}$ resolution, we re-sampled the

images on a 2400×2400 grid with a 0.0163 heliographic degrees pitch. Also, we used a radius of the Carrington projection sphere of 1.004R_{Sun} to minimize the average parallax over the FOV between the features observed by HRI$_{EUV}$ and AIA (Zhukov et al. 2021). Also, we used the SDO Helioseismic and Magnetic Imager (HMI) continuum images (14:35 UTC to 15:10 UTC) coaligned with AIA images to determine the supergranular cell boundaries.

3. Methods

Recently, Alipour et al. (2012) and Alipour & Safari (2015) investigated the feature detection methods based on machine learning and image processing for solar events (CBPs and minidimmings) observed by SDO/AIA images. ZMs provide unique and independent information for a class of features. In particular, ZMs for an event include abstractions of image information that reflect information on overall shape, geometrical, and morphological structure. Also, due to the Fourier term in Zernike polynomials, the absolute value of ZMs is invariant under rotation (Khotanzad & Hong 1990). Applying the image normalization, the ZMs will be translational and scaling invariant. This is done by transferring an image $I(x, y)$ into new image $I(x/a + x_{cm}, y/a + y_{cm})$ using the image centroid (x_{cm}, y_{cm}) and with a proper scale factor (a) (Raboonik et al. 2017). These bits of information about the content of a type of feature extracted by ZMs help us decide whether a solar sub-image exhibits an event or a non-event.

To detect CBPs from HRI$_{EUV}$ at 174 Å, we applied the previous CBPs automatic identification and tracking method (Alipour & Safari 2015) with some minor updates on the training set. Since HRI$_{EUV}$ at 174 Å and AIA at 171 Å campfires are tiny events, we develop an automatic feature detection method for campfires by collecting enough information on both campfires and non-campfires as the training database to feed into the SVM classifier. The automatic algorithm for campfires consists of two main parts: a joint campfire classifier (JCC:Sec 3.1) and a campfire detection method (Sec 3.2).

3.1. Joint campfire classifier

We collected (mainly by visual inspection) sub-images (for 700 events) that show signatures of tiny EUV brightenings in EUI images. We probed the EUI sequence images for events containing small-scale loops, elongated loops, loop apexes, and contact points between loops, collectively termed campfires, with lifetimes in the range of 10 to 200 s and with length scales ranging from 400 to 4000 km. For later convenience, brightening features with sizes larger than 4000 km are classified as CBPs. We took about 100 faint and small campfires, which were well identified by the wavelet automated detection method (Berghmans et al. 2021). Also, by visual inspection, we collected about 600 brightening features exhibiting the characteristics of these campfires. We also collected 700 sub-images for non-campfire features in the training set, including regions without campfires, some regions of large coronal loops, and so forth. In the next step, we computed the ZMs for campfires (positive class) and non-campfire (negative class) sub-images with five different sizes of $K_j \times K_j$ pixels ($j = 1 \cdots 5$, $K_1 = 13$, $K_2 = 17$, $K_3 = 19$, $K_4 = 23$, and $K_5 = 25$) for the maximum order number $P_{max} = 5$. For each of these five sub-images with different sizes, the ZMs with $P_{max} = 5$ has 21 data points placed in data set 1. We also generated ZMs with $P_{max} = 8$ (includes 45 data points) and five box
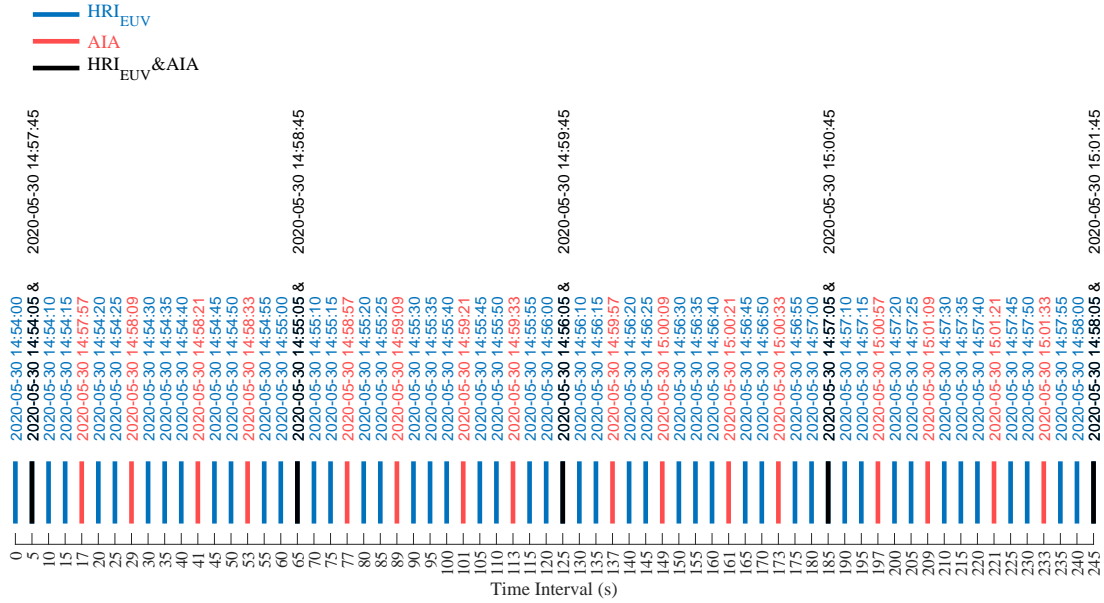

Fig. 1. Observation times for HRI$_{EUV}$ (blue lines), AIA (red lines), and simultaneously EUI and AIA (black lines). The first simultaneous image was observed by AIA at 2020-05-30 14:57:45 UTC and HRI$_{EUV}$ at 2020-05-30 14:54:05 UTC.

sizes for both positive and negative classes, which are located in data set 2. The main reason for using two different ZMs data sets is to ensure that the classifier can identify campfires with different data points. Also, the variety of campfire sizes is the reason for the use of sub-images of various sizes.

Figure 2 demonstrates a campfire and a non-campfire sub-image (with a size of 23×23 pixels) in original HRI$_{EUV}$ and reconstructed images with ZMs concerning $P_{max} = 5$ (red dashed line) and 8 (black line). The figure shows that the ZMs for the campfire and non-campfire are distinguishable. For the ZMs of a given campfire, some structures (e.g., blocks) and variations look different from non-campfire ZMs. If we select another campfire sub-image with different sizes and then compute the ZMs, the block structure is slightly similar, with minor differences to the ZMs of other campfires because it is the structure and variations similarity that is registered in the moments. These differences between ZMs of campfires and non-campfires give us confidence in applying a machine classifier (SVM) to identify features from HRI$_{EUV}$ and AIA images. In other words, the ZMs of two classes of features (campfires and non-campfires) in multidimensional feature space (the dimension of ZMs) have enough distributable information for a (statistically) learning machine to detect campfires.

We set the SVM classifier with Gaussian kernel parameter (rbf_sigma=15) in the training step to achieve a well-trained classifier. We randomly selected 70% of both positive and negative classes (for each ZMs data set 1 and 2) to apply as the training set. The remaining 30% of both classes was used as the test set. We used the same labels for both ZMs sets 1 and 2. In other words, we used two parallel classifiers for ZMs data set 1 (classifier 1) and ZMs data set 2 (classifier 2). We then compared the output of both classifiers. We consider a feature as a campfire if both classifiers have identified it in the positive class. Thus, we collected the respective labels for campfires and non-campfires in positive and negative classes as a joint campfire

classifier (JCC) component. Analyzing the output of the JCC, we evaluated the performance of automatic identification for campfires and non-campfires. To measure the performance of the campfire classification method, we applied various classification metrics. To do this, we use the elements of a confusion matrix (CM) in which the number of positive (P) and negative (N) features in the data set are terms of the CM (Powers 2011). The components of the CM are true positive (TP: campfires correctly recognized), false positive (FP: non-campfires incorrectly recognized), true negative (TN: non-campfires correctly recognized), and false negative (FN: campfires incorrectly recognized). The essential metrics are: precision, recall, f$_1$ score, accuracy, Gilbert Skill Score (GS), Heidke skill score (HSS$_1$, HSS$_2$), and the true skill statistic (TSS). The accuracy, precision, and f$_1$ are metrics for balanced class classifiers. In the test set of balanced class classifiers, the number of features and non-features are approximately the same. The HSS and GS metrics are also defined for the balanced class classifiers. However, the TSS is an essential metric to measure the performance of imbalanced class problems (Mason & Hoeksema 2010; Bloomfield et al. 2012; Barnes et al. 2016; Bobra & Couvidat 2015; Raboonik et al. 2017; Alipour & Safari 2015). Table 1 summarizes the metrics' formulae and their mean value for the joint classifier. The value of a given metric (e.g., TSS>0.8) shows that the classifier is well trained with acceptable performance to identify campfires.

3.2. Identification and tracking of campfires

We applied the JCC to identify campfires from EUI images. Figure 3 shows a schematic flowchart for the identification of campfires in each EUI image. The algorithm automatically scans a EUI image by a moving box. For each HRI$_{EUV}$ image, starting from $x = 13$ and $y = 13$, we extracted a small region with size $\Delta x = \Delta y = 4$. We applied the joint campfire classifier to identify campfires from the EUI images. We determined
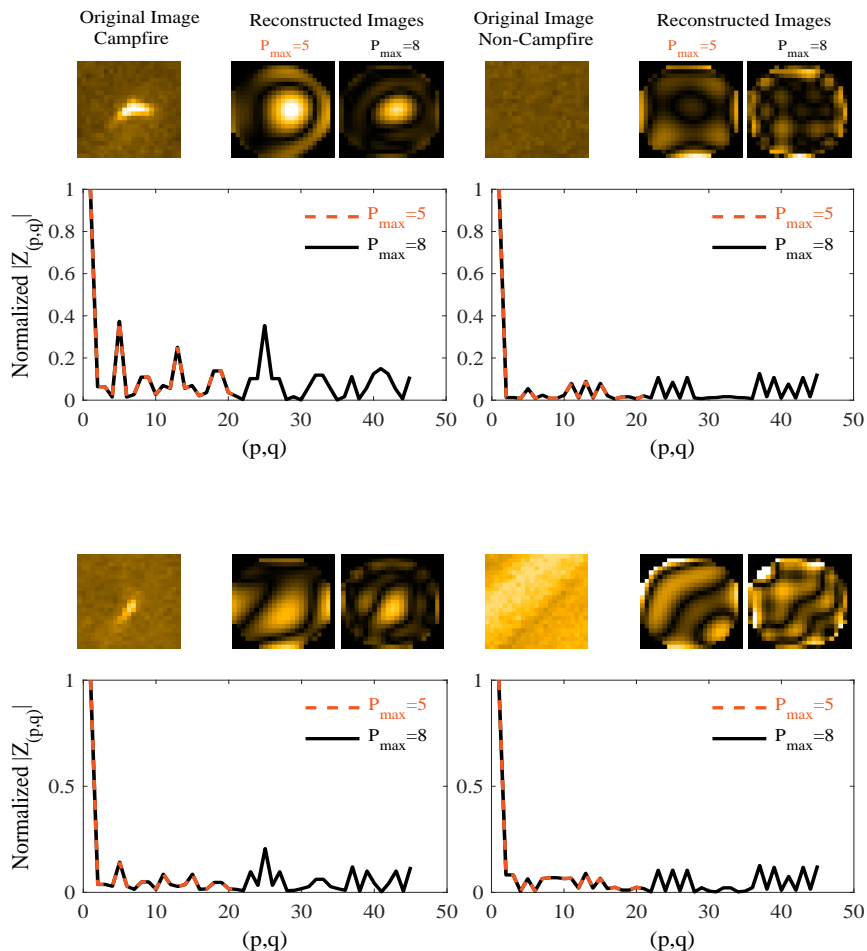
Fig. 2. Original HRI$_{EUV}$ images, reconstructed images, and ZMs in relation to P_{max} = 5 (red dashed line) and 8 (black line) for two campfires (left panel) and two non-campfires (right panel). The order, p, is a non-negative integer and repetition, q, is an integer ($|q| - p \leq 0$ is an even number). For a given maximum order (P_{max}), the pair (p, q) is labeled from 1 to $\sum_{p=0}^{P_{max}} (p + 1)$ (Alipour et al. 2019).

the position, x_c, and y_c, of the maximum intensity inside the small region. This gives the location of the brightest pixel in the small region. In the next step, we selected larger region square boxes around the maximum intensity position with sizes $\Delta x \times \Delta y = K_j \times K_j$ ($j = 1 \cdots 5$) pixels. The ZMs (for both P_{max} = 5 and 8) of these sub-images are computed. Then, the magnitudes of ZMs are fed to the JCC. The JCC picks up a label of 1 for a campfire candidate and 2 for a non-campfire sub-image. We applied a region growing (RG) function to the sub-image to extract the bright pixels. We consider the candidate a campfire if the linear length is greater than one pixel and smaller than 20 pixels. The image number (time) and output of the RG function for each campfire are saved. Then we move the small box first in x direction up to the end of the grid and then in y direction.

In the next step, we performed a tracking algorithm in the sequence of EUI images to obtain the duration of campfires. The algorithm tracks the identified campfires in the sequential HRI$_{EUV}$ images with an intersection of regions (joint pixels). To do this, we compared the locations (pixels) of the campfires at times t_i (i is the image number) and t_{i+1} for all HRI$_{EUV}$ images.

Next, we marked campfires with an intersection of regions (joint pixels in the sequence of images) with the same labels. Then, using the labels and their related times, we computed the duration of campfires.

4. Results

4.1. HRI$_{EUV}$ brightenings

We applied the automatic identification and tracking method for brightening features (CBPs and campfires) to the sequence of 50 Carrington projected HRI$_{EUV}$ images. Supplement S1 provides the sequence of 50 EUI at 174 Å images and the location of maximum intensity and time for the identified campfires as MATLAB structures. Supplement S2 gives movies for tracked campfires with the contour and label for each.

Figure 4 represents an HRI$_{EUV}$ image with 449 detected campfires (cyan contours) and 240 CBPs (purple contours), within which 149 campfires were observed. We found that 27% of campfires occurred inside CBPs. In other words, these camp-
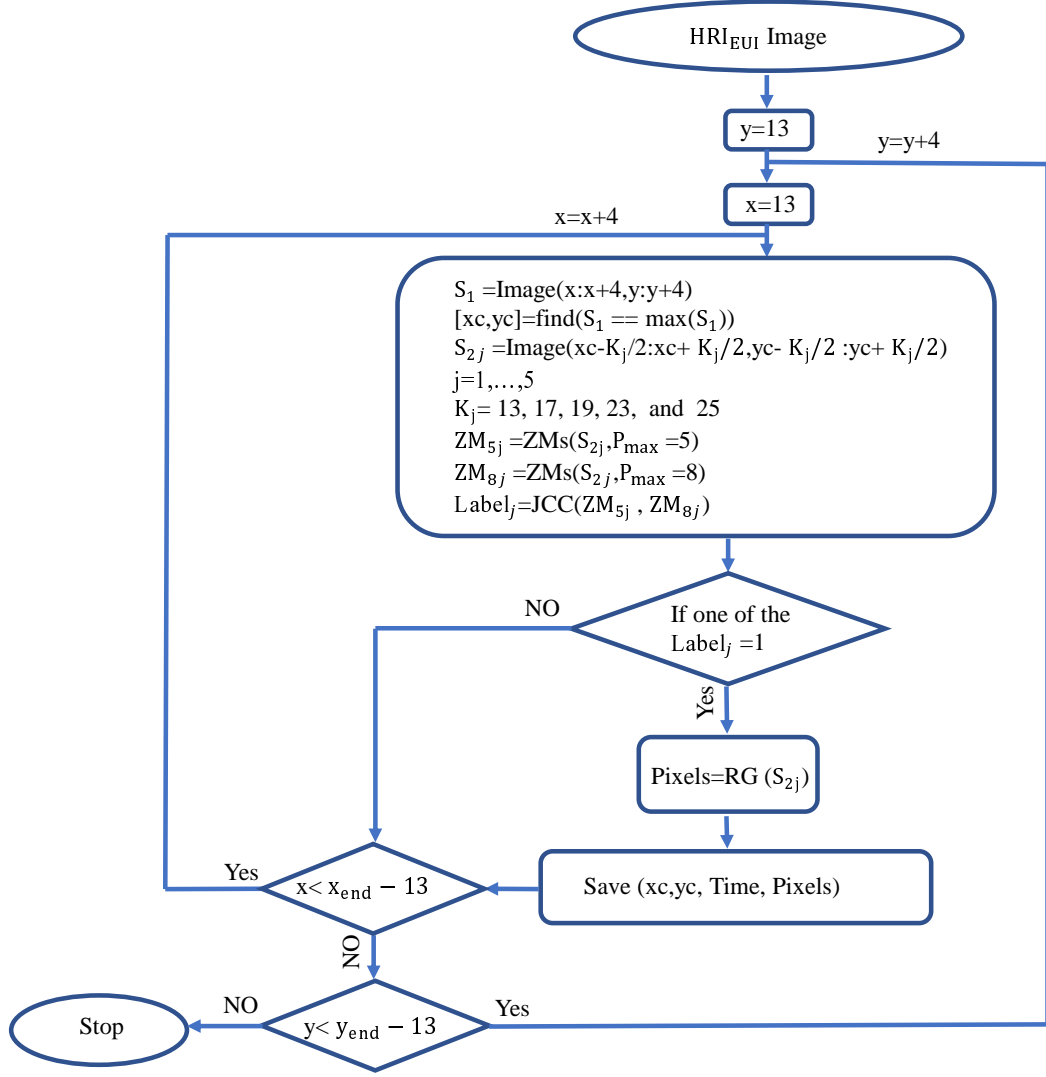
```
                    HRI_EUI Image

                         │
                    ┌─────────┐           y=y+4
                    │  y=13   │
                    └─────────┘
                         │
                    ┌─────────┐
                    │  x=13   │
                    └─────────┘
    x=x+4                │
┌──────────────────────────────────────────────┐
│  S₁ =Image(x:x+4,y:y+4)                        │
│  [xc,yc]=find(S₁ == max(S₁))                   │
│  S₂ⱼ =Image(xc-Kⱼ/2:xc+ Kⱼ/2,yc- Kⱼ/2 :yc+ Kⱼ/2) │
│  j=1,…,5                                        │
│  Kⱼ= 13, 17, 19, 23,  and  25                  │
│  ZM₅ⱼ =ZMs(S₂ⱼ,P_max =5)                       │
│  ZM₈ⱼ =ZMs(S₂ⱼ,P_max =8)                       │
│  Labelⱼ=JCC(ZM₅ⱼ , ZM₈ⱼ)                       │
└──────────────────────────────────────────────┘
```

$S_1 = \text{Image}(x{:}x{+}4, y{:}y{+}4)$

$[xc, yc] = \text{find}(S_1 == \max(S_1))$

$S_{2j} = \text{Image}(xc{-}K_j/2{:}xc{+}K_j/2, yc{-}K_j/2{:}yc{+}K_j/2)$

$j = 1,\dots,5$

$K_j = 13, 17, 19, 23, \text{ and } 25$

$ZM_{5j} = ZMs(S_{2j}, P_{max} = 5)$

$ZM_{8j} = ZMs(S_{2j}, P_{max} = 8)$

$\text{Label}_j = JCC(ZM_{5j}, ZM_{8j})$

Decision: **If one of the $\text{Label}_j = 1$** — NO → ; Yes ↓

$\text{Pixels} = RG(S_{2j})$

Save (xc,yc, Time, Pixels)

Decision: $x < x_{end} - 13$ — Yes → ; NO ↓

Decision: $y < y_{end} - 13$ — Yes → (y=y+4); NO → Stop

Fig. 3. Schematic flowchart for identification of HRI_EUV and AIA campfires .

fires were hosted within CBPs and the remaining 73% were observed out-of-CBPs.

We detected 8678 campfires with length scales larger than or equal ($\geq$) 400 km and smaller than 4000 km. This gives a campfire birthrate of about $2 \times 10^{-16} \text{m}^{-2}\text{s}^{-1}$. The number of events and their birthrate determined by the present method is approximately 5.4 times larger than those obtained using the wavelet detection scheme (Berghmans et al. 2021). Interestingly, the derived campfire birthrate is of the same order of magnitude as that found for explosive events (Teriaca et al. 2004), which required more investigation for the relationship between the two events. The wavelet detection scheme as pattern recognition is one dependent on the threshold used that detects a different number of events with changing the threshold value. After some minor modifications of the wavelet detection algorithm to work in space (x, y) and time (t), the method was applicable for denoising images and identifying more campfires. However, the present campfires detection as a machine learning method identifies an event inside a sub-image with the specific characteristics in the feature space provided by ZMs. Figure 5 shows a campfire at the original, artificial Gaussian, and salt-pepper noises together with ZMs and their reconstructed images. We find that ZMs are less sensitive to noise, as the reconstructed images are approximately the same for various types of noise. This is one of the reasons that we used ZMs instead of original images in feature space. We note that our training positive class contains the information of sub-images in which each sub-image has an event with a linear length greater than 400 km and smaller than 4000 km and lifetimes of more than 10 s. This implies that we have chosen the suitable training features for the campfire class, excluding the noise features. However, the negative class may contain many non-campfire and noise features that do not have campfire characteristics. Since the training feature space contains the morphology, structure, shape, and other information on the event, a detected single-frame event is considered a campfire if it consists of the bright pixel(s) and the neighboring pixels. In other words, for a sub-image that contains some individual or group of bright pixels without the characteristics of campfires in the feature space (ZMs), it will be classified as a non-campfire.

Of the 8678 detected campfires, 3300 have lifetimes larger than 5 s and less than 245 s. We observed 23 campfires with a duration longer than 245 s. Figure 6 shows three tracked samples with lifetimes in the range of 15 s to 25 s (campfire 1, top row), 10 s to 20 s (campfire 2, middle row), and 5 s to 15 s (campfire 3,

Table 1. Definitions of various skill scores as the measure for the performance of classifier and their mean values for campfires.

Score	Formula	Campfires
Recall (positive)	$\mathrm{recall}^+ = \dfrac{\mathrm{TP}}{\mathrm{TP} + \mathrm{FN}}$	0.92 ± 0.02
Recall (negative)	$\mathrm{recall}^- = \dfrac{\mathrm{TN}}{\mathrm{TN} + \mathrm{FP}}$	0.93 ± 0.02
Precision (positive)	$\mathrm{precision}^+ = \dfrac{\mathrm{TP}}{\mathrm{TP} + \mathrm{FP}}$	0.93 ± 0.02
Precision (negative)	$\mathrm{precision}^- = \dfrac{\mathrm{TN}}{\mathrm{TN} + \mathrm{FN}}$	0.92 ± 0.02
f_1 score (positive)	$f1^+ = \dfrac{2 \times \mathrm{precision}^+ \times \mathrm{recall}^+}{\mathrm{precision}^+ + \mathrm{recall}^+}$	0.92 ± 0.01
f_1 score (negative)	$f1^- = \dfrac{2 \times \mathrm{precision}^- \times \mathrm{recall}^-}{\mathrm{precision}^- + \mathrm{recall}^-}$	0.93 ± 0.01
Accuracy	$\mathrm{accuracy} = \dfrac{\mathrm{TP} + \mathrm{TN}}{\mathrm{TP} + \mathrm{FN} + \mathrm{TN} + \mathrm{FP}}$	0.93 ± 0.01
Heidke Skill Score (HSS1)	$\mathrm{HSS}_1 = \dfrac{\mathrm{TP} - \mathrm{FP}}{\mathrm{TP} + \mathrm{FN}}$	0.85 ± 0.02
Heidke Skill Score (HSS2)	$\mathrm{HSS}_2 = \dfrac{2 \times [(\mathrm{TP} \times \mathrm{TN}) - (\mathrm{FN} \times \mathrm{FP})]}{(\mathrm{TP} + \mathrm{FN}) \times (\mathrm{FN} + \mathrm{TN}) + (\mathrm{TN} + \mathrm{FP}) \times (\mathrm{TP} + \mathrm{FP})}$	0.85 ± 0.02
Gilbert Skill Score (GS)	$\mathrm{GS} = \dfrac{\mathrm{TP} - \mathrm{CH}}{\mathrm{TP} + \mathrm{FP} + \mathrm{FN} - \mathrm{CH}}$, $\mathrm{CH} = \dfrac{(\mathrm{TP} + \mathrm{FP}) \times (\mathrm{TP} + \mathrm{FN})}{\mathrm{TP} + \mathrm{FN} + \mathrm{TN} + \mathrm{FP}}$	0.74 ± 0.04
True Skill Statistic (TSS)	$\mathrm{TSS} = \dfrac{\mathrm{TP}}{\mathrm{TP} + \mathrm{FN}} - \dfrac{\mathrm{FP}}{\mathrm{FP} + \mathrm{TN}}$	0.85 ± 0.02

EUI 2020-05-30 14:54:05 UTC
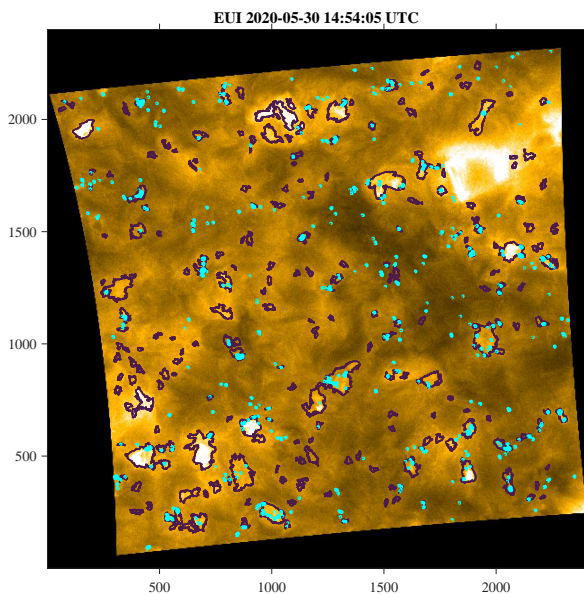
Fig. 4. $\mathrm{HRI_{EUV}}$ image at 174 Å on 30 May 2020 14:54:05 UTC projected to Carrington coordinates. The code detected 240 coronal bright points (CBPs: purple contours) and 449 campfires (cyan contours).

bottom row). Some factors such as identification errors (perfor-

mance scores in Table 1), displacement of the bright pixels, and variation of the length scale for some campfires may affect the number of detected campfires. We found that the tracking algorithm suffers the false negative error in which the actual number of events is probably more than the detected campfires. Therefore, this affects the duration of detected events, and the actual lifetime for some campfires is more than the values mentioned above. So, the 3300 campfires with a duration of at least 5 s are the lower limit for this algorithm.

A campfire's intensity in $\mathrm{HRI_{EUV}}$ is computed by integrating all corresponding pixel values at each image. The peak intensity is the maximum intensity during the observed campfire duration. The total intensity of an event obtains the summing of the intensity over the whole duration. Figure 7 shows the position of 8678 campfires, supergranular boundaries, an average of 50 $\mathrm{HRI_{Lya}}$images, and the frequency of campfires' (centroid) shortest distances from the supergranular boundaries for $\mathrm{HRI_{Lya}}$ intensity. To determine the supergranular boundaries, we applied the ball tracking method on the respective SDO/HMI continuum images (Potts et al. 2004; Attie & Innes 2015; Attie et al. 2016) for tracking solar photospheric flows. The shortest distance of a campfire centroid (center of brightness in $\mathrm{HRI_{EUV}}$) from supergranular boundaries is computed. We observed that campfires with a higher total intensity were mostly placed at supergranular junctions and high $\mathrm{HRI_{Lya}}$ emission regions. We found that most (80%) of campfires are placed near supergranular boundaries (Fig. 7a). In other words, about 80% of the events have the shortest distances (minimum distance of a
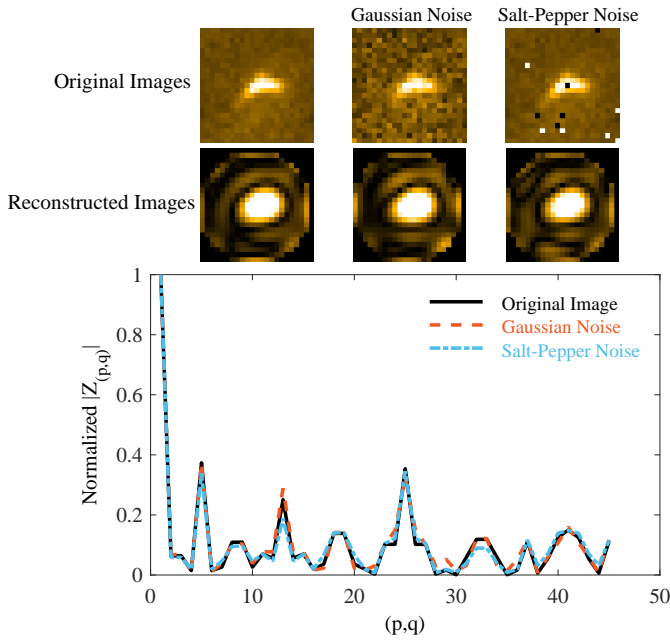
Fig. 5. Campfire at the original, artificial Gaussian, and salt-pepper noises (upper row) together with the reconstructed images (middle row) and their ZMs (bottom row).
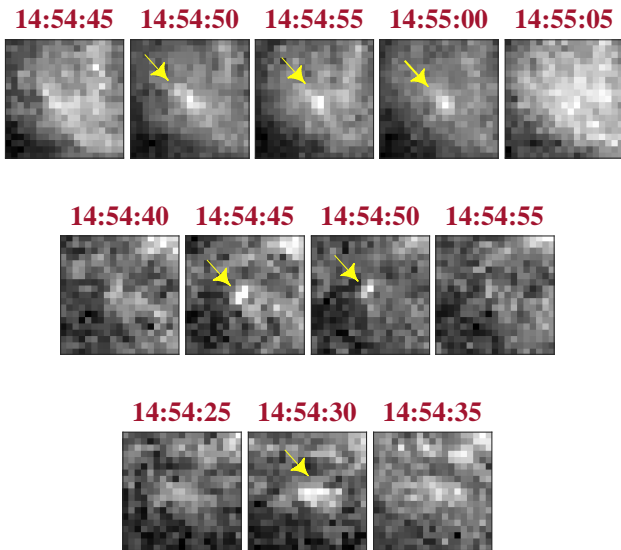

Fig. 6. Three tracked samples with duration in the range of 15 s to 25 s (campfire 1, top row), 10 s to 20 s (campfire 2, middle row), and 5 s to 15 s (campfire 3, bottom row).

Fig. 7. (a) Position of 8678 campfires (color dots: the total intensity of campfires) and supergranular boundaries (white lines). The color map indicates the pixels' integrated intensity of campfires. (b) Average of 50 HRI_{Lya} images, supergranular boundaries (white lines), and position of campfires (green dots). (c) Frequency (number) of campfires' shortest distances (distance (D) of campfires centroid from the supergranular boundaries) for HRI_{Lya} intensity <400 DN/s (blue line), 400 to 900 DN/s (black line), and > 900 DN/s (red line). About 2/3 of campfires have the HRI_{Lya} intensity of the centroid in the range of 400 to 900 DN/s.

campfire centroid from the nearest supergranular boundaries) less than 5 Mm. The typical diameter of solar supergranules is significantly larger than 20 Mm (e.g., Del Moro et al. 2004; Noori et al. 2019). About 2/3 of campfires have the HRI_{Lya} intensity of the centroid in the range of 400 to 900 DN/s (Fig. 7b-c). We also found that the high HRI_{Lya} intensities were distributed around the supergranular boundaries (Fig. 7b). The supergranular boundaries are the places for a high concentration of magnetic fields and converging photospheric flows (Priest 2014). As we observed, campfires are short-lived features similar to other types of small-scale transients: explosive events (Porter & Dere 1991), CBPs (Yousefzadeh et al. 2016; Madjarska 2019), mini-coronal mass ejections (Honarbakhsh et al. 2016), and blinkers (Harrison 1997; Shokri et al. 2022). These are predominantly localized and analogous to those of flaring events (with a different

amount of the involved energy). Panesar et al. (2021) showed that most of the 52 campfires in their investigation were above magnetic neutral lines with a considerable rate of flux cancelation (van Ballegooijen & Martens 1989), which indicates that flux cancelation (i.e., an inherently resistive, magnetic reconnection mechanism) could be the primary mechanism in the formation of campfires. Therefore, it might be possible to hypothesize that campfires are flare-like events, but on a vastly smaller scale (e.g., Giovanelli 1946; Dungey 1953). This hypothesis needs to be investigated in further detail.

Figure 8 shows the probability distribution function (PDF) and complementary cumulative distribution function (CCDF) of the total intensity (first row), peak (maximum) intensity (second row), projected area (third row), and duration (fourth row) of campfires (black lines). To obtain the projected area for a campfire, we used every pixel area that a campfire occupies at some stage during its duration (Berghmans et al. 2021). As shown in the figure, the distributions show heavy-tailed behaviors. The power law and lognormal distributions are well-known distributions for modeling of such heavy-tailed flaring events (Lin et al. 1984; Crosby et al. 1993; Krucker & Benz 1998; Parnell & Jupp 2000; Pauluhn & Solanki 2007a; Bazarghan et al. 2008; Klimchuk et al. 2009; Tajfirouze & Safari 2012; Farhang et al. 2019; Verbeeck et al. 2019). The power law distribution function is

$$\text{PDF}(x, x_{\min}, \alpha) = \frac{\alpha - 1}{x_{\min}} \left(\frac{x}{x_{\min}} \right)^{-\alpha}, \quad (1)$$

where $x_{\min}$ is the cut-off and α is the power law index. To determine the minimum value for the cut-off ($x_{\min}$), we first create a power law fit that begins from a unique guess cut-off within the data. Then, the minimization of the distance between the data and power law fit guides to select the optimal value for $x_{\min}$ (Clauset et al. 2009a). The lognormal function is

$$\text{PDF}(x, \mu, \sigma) = \frac{1}{x\sigma\sqrt{2\pi}} \exp\left(-\frac{(\ln x - \mu)^2}{2\sigma^2} \right), \quad (2)$$

where μ is the mean and σ is the shape parameter.

We applied a maximum-likelihood approach (Clauset et al. 2009b) for fitting the power law and lognormal distributions to the total intensity, peak intensity, projected area, and duration for campfires. We applied a hypothesis test via Kolmogorov–Smirnov statistic that the null hypothesis supposes no significant difference between the observational distribution and the desired model. Instead, the alternative hypothesis supposes a significant difference between the observation and the model. Calculating a p-value, we can decide whether the model hypothesis is plausible for our data or not. A p-value smaller than 0.1 refutes the null hypothesis indicating that the specific model is ruled out (Mayo & Cox 2006). In contrast, we cannot refute the null for a p-value greater than 0.1. Using the bootstrapping approach, we determined the uncertainty and true value of the parameters for both the power law and lognormal distributions.

Table 2 shows the p-values and fit parameters for power law and lognormal distributions (Fig. 8) of the total intensity, peak intensity, area, and duration for the campfires. The p-values larger than 0.1 for both the power law and lognormal models mean we could not reject these models for the total intensity, peak intensity, projected area, and duration distributions. As expected, the lognormal distribution is a simpler explanation for most data because the power law distribution only has

a fit parameter (α) and the lognormal model has two fit parameters (μ, σ). However, in rare cases, a power law may be a better fit than a lognormal distribution if the data is inherently generated by mechanisms that obey a power law model. Multiplying random positive variables together is a simple mechanism for generating a lognormal distribution. However, the preferential attachment (Gheibi et al. 2017) and cellular automaton avalanche models (Lu et al. 1993; Farhang et al. 2019) are examples of generation mechanisms of a power law distribution. Pauluhn & Solanki (2007a) developed a model to simulate the nanoflare emissions observed by the Solar and Heliospheric Observatory (SOHO)/Solar Ultraviolet Measurements of Emitted Radiation (SUMER). In their model, an initial kick is generated by a power law distribution and evaluated by a multiplicative random process. The distribution of the resultant energies obeys a lognormal distribution, which saved the power law property in the memory of light curves. To determine the power law index for such light curves (e.g., small-scale emissions observed by SUMER and AIA), Bazarghan et al. (2008); Tajfirouze & Safari (2012); Upendran & Tripathi (2021) developed methods based on neural networks.

We obtained a power law index of about 2.1±0.1, 2.7±0.05, 3.0±0.05, and 2.6±0.05 for the total intensity, peak intensity, projected area, and duration (Fig. 8), respectively. The power law index (for peak intensity and total intensity of campfires as a class of small-scale events) greater than 2 is in agreement with the previous findings for energetic events (e.g., Krucker & Benz 1998; Pauluhn & Solanki 2007b; Bazarghan et al. 2008; Tajfirouze & Safari 2012; Reale 2014). Furthermore, the power law index of about 2.7 for the peak intensity distribution of campfires is in the range of indices obtained for the distribution of energy-loss flux of CBPs (Hosseini Rad et al. 2021). Generally, however, when deriving a power law index, there are error sources such as the instrument sensitivity, performance of a feature detection method (identification and tracking), estimation of modeling parameters, and the specific time of observations at a solar cycle (e.g., Parnell & Jupp 2000; Parnell 2002; Hosseini Rad et al. 2021). An accurate determination of the power law index for the energy distribution of flaring-like instabilities (from picoflares to large X-class flares) and their generating mechanisms is still an open problem (Verbeeck et al. 2019). Nevertheless, the power law behaviors may result from the self-similar features such as magnetic reconnection that generates campfires, similarly to magnetic field instabilities of self-organized criticality (Lin et al. 1984; Crosby et al. 1993; Aletti et al. 2000; Georgoulis et al. 2001; Parenti et al. 2006; Klimchuk et al. 2009; McAteer et al. 2016; Aschwanden et al. 2016; Farhang et al. 2018).

4.2. Comparing AIA and HRI$_{\text{EUV}}$ campfires

To compare the campfires observed in AIA 171 Å images with the same FOV as HRI$_{\text{EUV}}$ 174 Å images, first we identified features in the original AIA images based on JCC. To do this, we used a moving box (Appendix 3.1 and 3.2) with sizes slightly larger than half of the moving boxes for HRI$_{\text{EUV}}$ due to the different resolution of the two instruments. Then we remapped the images to Carrington coordinates. Fig. 9 shows an AIA 171 Å image (remapped to Carrington coordinates) with 147 campfires (cyan contours). At AIA's 12 s cadence, 21 images are available during the HRI$_{\text{EUV}}$ image sequence (at the same FOV as HRI$_{\text{EUV}}$). For AIA images, the method picked up 1131 campfires. As one output of the classifier, we observed that the camp-
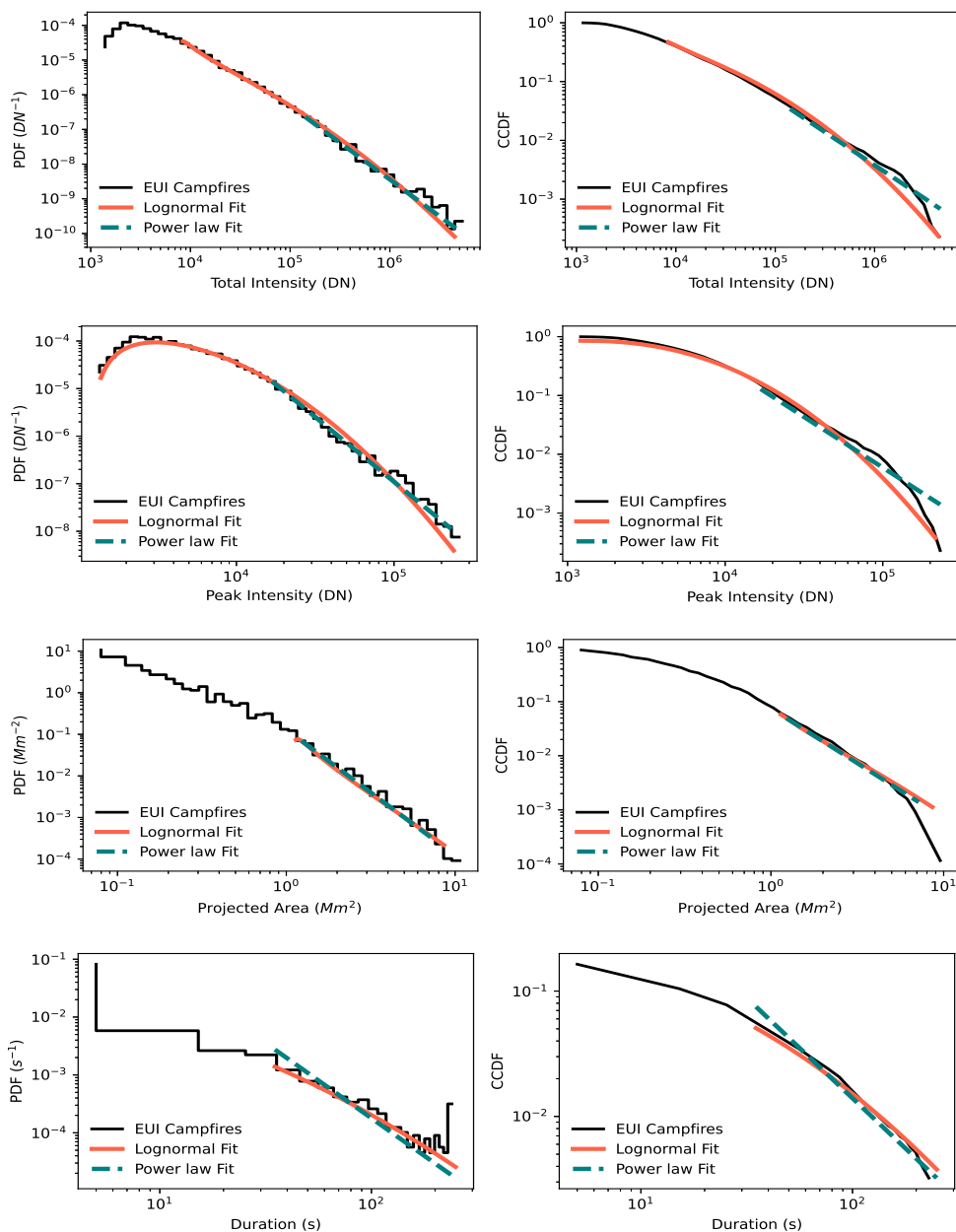
Fig. 8. Probability distribution function (PDF; left column) and complementary cumulative distribution function (CCDF; right column) of the total intensity (first row), peak intensity (second row), projected area (third row), and duration (fourth row) of campfires observed by HRI$_{EUV}$ (black line). Power laws (power law fit: blue dashed lines) and lognormal functions (lognormal fit: red line) are fitted to each distribution.

fire sub-images consist of at least two or more bright pixels (with linear length scale $\geq$880 km). We also observed that CBPs hosted about 48% of the campfires. We observed about 500 campfires detected in at least a sequence of two AIA images. Comparing the positions and times of features, we found that 50% of the campfires observed in 21 AIA images were also detected in HRI$_{EUV}$ at 174 Å images (e.g., Figs. 4 and 9). However, about 16% of campfires detected in HRI$_{EUV}$ images were observed at AIA images. These differences in the number of campfires detected by AIA and HRI$_{EUV}$ may be related to the different spatial resolution due to the different heliocentric distances. At 0.556 AU from the Sun, EUI provides a spatial resolution of about 198 km, slightly less than half of AIA. These differences between the two analyses may be related to the slight differences in the AIA 171 Å and HRI$_{EUV}$ 174 Å bandpasses. A portion of these

differences may relate to the different sizes of a feature in AIA and EUI, which are determined via a region-growing approach. In other words, some of the campfires detected in AIA with a length scale of about 4000 km have slightly larger length scales in EUI observations, so they were not considered as EUI campfires. Also, due to differences in the spatial resolution of the two instruments, we considered different lower limits on the length scale of campfires of about two pixels in both instruments (about 400 km at EUI and 880 km at AIA) to avoid the detection of the noise features.

Figure 10 shows a campfire (supplement S3 movie) observed by HRI$_{EUV}$ (first three images) and AIA (two last images) from left to right. The duration of this campfire was greater than 245 s in the HRI$_{EUV}$ images re-mapped to Carrington coordinates with

Table 2. Parameters and p-values of fitted power law and lognormal distributions for peak intensity, total intensity, projected area, and duration of campfires.

Dataset	Power law		Lognormal		
	α	p-value	μ	σ	p-value
Total Intensity	2.13 ± 0.1	0.7	$9.40. \pm 0.02$	1.78 ± 0.01	0.2
Peak Intensity	2.72 ± 0.05	0.4	8.72 ± 0.01	1.06 ± 0.01	0.2
Area Projected	3.02 ± 0.12	0.2	-0.78 ± 0.06	1.34 ± 0.04	0.2
Duration	2.62 ± 0.05	0.2	0.83 ± 0.06	1.53 ± 0.07	0.8
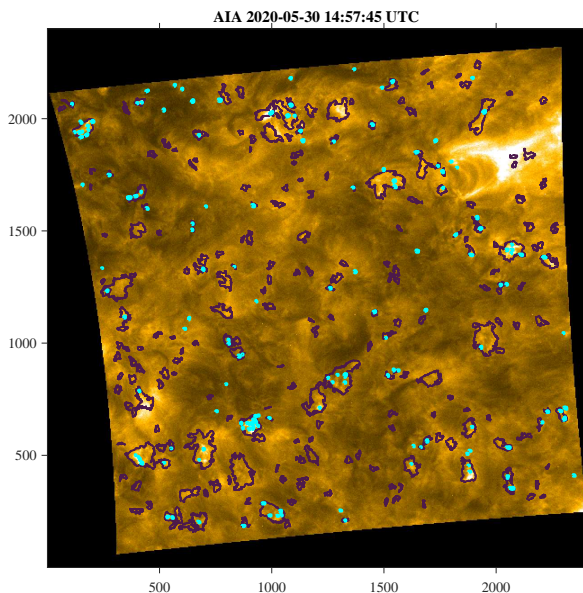
Fig. 9. Positions of 147 campfires (cyan contours) in an AIA 171 Å image re-mapped to Carrington coordinates. The positions of 240 CBPs (purple contours) are shown.

the same region as the AIA images. We detected this campfire in the AIA images with a duration greater than 293 s.

5. Conclusions

In this work, we apply machine learning-based automatic identification and tracking algorithms for CBPs and campfires to a sequence of 50 HRI$_{EUV}$ at 174 Å and 21 AIA at 171 Å images recorded on 30 May 2020. The method uses information on features provided by ZMs that is fed into the SVM classifier to identify brightening features. The joint campfire classifier (JCC), as the combination of several SVM classifiers, uses a variety of information extracted with different moving box sizes and two maximum order numbers (P_{max} = 5 and 8) for ZMs to detect campfires from both HRI$_{EUV}$ and AIA images. We measured the performance metric of the JCC machine (Table 1), which shows that the machine is well trained to identify the campfires. The tracking algorithm applied the RG function to extract bright pixels and followed events with the joint pixels through the sequence of images.

We detected 8678 campfires with a birthrate of about $2 \times 10^{-16} m^{-2} s^{-1}$ in HRI$_{EUV}$ images. About 3300 campfires have a duration longer than 10 s, among which 23 campfires have a duration longer than 245 s (the last point at the tail of the duration PDF in Fig. 8). Due to the false-negative error (i.e., erroneously

identifying some of the campfire features as non-campfires) of the JCC machine for campfires, the 3300 events with a duration of more than 10 s is a lower limit for the detection algorithm. It may well be possible that the actual number of campfires and their birthrate are higher than those identified by the present algorithm. In addition, CBPs hosted about 27% of campfires and the rest occurred out of CBPs. By applying the JCC machine to 21 AIA images (the same FOV of HRI$_{EUV}$ images), we observed 1131 campfires with the linear length scale approximately in the range of 880 km to 4000 km. We observed that 500 campfires have a duration in the range of 12 s to 264 s. We compared the AIA and HRI$_{EUV}$ features (e.g., Figs. 4 and 9) that show about 50% of the campfires observed in AIA were also identified in HRI$_{EUV}$. In contrast, about 16% of campfires recognized in HRI$_{EUV}$ were detected in AIA data.

Due to the differences in the spatial resolution of the two instruments, the tiny HRI$_{EUV}$ brightenings may appear weaker and fuzzier (i.e., very close to the background oscillations) in the AIA observations; hence, we presume that they were not detected by this classifier machine. This may imply that achieving observations of higher spatial resolution (i.e., closer Solar Orbiter perihelia) will give rise to (perhaps even significantly) more campfire detections. Another reason may be related to the differences of 174 Å of HRI$_{EUV}$ and 171 Å of AIA observations. Tiwari et al. (2019) observed Hi-C brightening features for active regions that were bigger than HRI$_{EUV}$ś campfires. Joulin et al. (2016) and Chitta et al. (2021) studied the quiet-Sun small-scale brightening EUV events with SDO/AIA. The present method may provide accurate detections of smaller brightenings for HRI$_{EUV}$ at heliocentric distances < 0.3 AU, so that the role of these events in the dynamics and, possibly, heating of the solar corona may be investigated in greater detail(Berghmans et al. 2021).

Using a maximum likelihood estimation, we determined a power law index of about 2.1±0.05, 2.7±0.04, 3.0±0.05, and 2.6±0.05, respectively, for the distribution of the total intensity, peak intensity, projected area, and duration. The power law behavior is one of the primary characteristics of self-organized criticality systems such as flaring events (Lu et al. 1993; Vlahos et al. 1995; Strugarek & Charbonneau 2014; McAteer et al. 2016; Aschwanden et al. 2016, 2018; Farhang et al. 2019). However, there are no unique reports for the power law index of flaring events and the variety of power law indexes ranging from 1.5 to 2.16 (e.g., Hudson 1991; Georgoulis & Vlahos 1998; Veronig et al. 2002; Aschwanden & Freeland 2012) and 1.5 to 2.7 (e.g., Krucker & Benz 1998; Berghmans & Clette 1999; Hosseini Rad et al. 2021) for large flares (M- and X- class) and small-scale flares (nanoflares, microflares, etc.), respectively, have been widely reported. This self-similar (or scale-free) property may shed light on the triggering process of campfires. In this context, recent studies of Panesar et al. (2021) and Kahil et al.
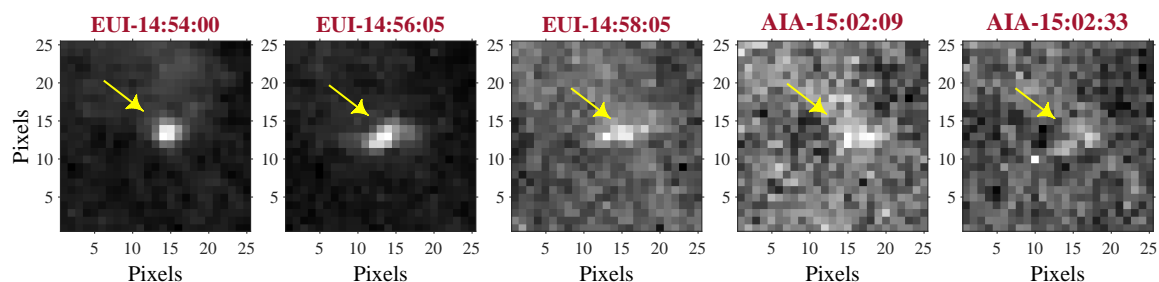
Fig. 10. Campfire (supplement S3 movie, label 63) was observed by both HRI$_{EUV}$ (position: x=737,y=1539 in Figure 4) and AIA (two latest sub-image at final stage). Its duration was more than 245 s in the EUI (14:54:00 to 14:58:05 UTC) observations. The actual duration in the range of 293 s to 312 s was observed in AIA images. The difference in light travel time of 220 s needs to be considered between the two spacecraft.

(2022) show that a majority of campfires are associated with the cancelation of magnetic flux in the photosphere. We showed that the majority of HRI$_{EUV}$ campfires were placed at regions of intense HRI$_{Lya}$emission and supergranular boundaries (lanes and junctions). We determined the supergranular boundaries by applying the ball-tracking method on the SDO/HMI images (Fig. 7). About 2/3 of campfires have their HRI$_{Lya}$ intensity (for the centroid) in the range of 400 to 900 DN/s. These pieces of evidence, along with the accumulation of campfires above network boundaries and neutral lines, suggest that magnetic reconnection may be considered an essential mechanism in the formation of campfires as dynamically evolving episodes of energy release.

References

Aletti, V., Velli, M., Bocchialini, K., et al. 2000, ApJ, 544, 550
Alipour, N., Mohammadi, F., & Safari, H. 2019, ApJS, 243, 20
Alipour, N. & Safari, H. 2015, ApJ, 807, 175
Alipour, N., Safari, H., & Innes, D. E. 2012, ApJ, 746, 12
Aschwanden, M. J., Crosby, N. B., Dimitropoulou, M., et al. 2016, Space Sci. Rev., 198, 47
Aschwanden, M. J. & Freeland, S. L. 2012, ApJ, 754, 112
Aschwanden, M. J., Scholkmann, F., Béthune, W., et al. 2018, Space Sci. Rev., 214, 55
Attie, R. & Innes, D. E. 2015, A&A, 574, A106
Attie, R., Innes, D. E., Solanki, S. K., & Glassmeier, K. H. 2016, A&A, 596, A15
Barnes, G., Leka, K. D., Schrijver, C. J., et al. 2016, ApJ, 829, 89
Bazarghan, M., Safari, H., Innes, D. E., Karami, E., & Solanki, S. K. 2008, A&A, 492, L13
Berghmans, D., Auchère, F., Long, D. M., et al. 2021, A&A, 656, L4
Berghmans, D. & Clette, F. 1999, Sol. Phys., 186, 207

Bloomfield, D. S., Higgins, P. A., McAteer, R. T. J., & Gallagher, P. T. 2012, ApJ, 747, L41
Bobra, M. G. & Couvidat, S. 2015, ApJ, 798, 135
Chen, Y., Przybylski, D., Peter, H., et al. 2021, arXiv e-prints, arXiv:2104.10940
Chitta, L. P., Peter, H., & Young, P. R. 2021, A&A, 647, A159
Clauset, A., Shalizi, C. R., & Newman, M. E. J. 2009a, SIAM Review, 51, 661
Clauset, A., Shalizi, C. R., & Newman, M. E. J. 2009b, SIAM Review, 51, 661
Crosby, N. B., Aschwanden, M. J., & Dennis, B. R. 1993, Sol. Phys., 143, 275
Del Moro, D., Berrilli, F., Duvall, T. L., J., & Kosovichev, A. G. 2004, Sol. Phys., 221, 23
Dungey, J. W. 1953, The London, Edinburgh, and Dublin Philosophical Magazine and Journal of Science, 44, 725
Farhang, N., Safari, H., & Wheatland, M. S. 2018, ApJ, 859, 41
Farhang, N., Wheatland, M. S., & Safari, H. 2019, ApJ, 883, L20
Georgoulis, M. K., Vilmer, N., & Crosby, N. B. 2001, A&A, 367, 326
Georgoulis, M. K. & Vlahos, L. 1998, A&A, 336, 721
Gheibi, A., Safari, H., & Javaherian, M. 2017, ApJ, 847, 115
Giovanelli, R. G. 1946, Nature, 158, 81
Golub, L., Krieger, A. S., Silk, J. K., Timothy, A. F., & Vaiana, G. S. 1974, ApJ, 189, L93
Harrison, R. A. 1997, Sol. Phys., 175, 467
Honarbakhsh, L., Alipour, N., & Safari, H. 2016, Sol. Phys., 291, 941
Hosseini Rad, S., Alipour, N., & Safari, H. 2021, ApJ, 906, 59
Hsu, C.-C., Wang, K.-S., & Chang, S.-H. 2011, Expert Systems with Applications, 38, 4698
Hudson, H. S. 1991, Sol. Phys., 133, 357
Joulin, V., Buchlin, E., Solomon, J., & Guennou, C. 2016, A&A, 591, A148
Kahil, F., Hirzberger, J., Solanki, S. K., et al. 2022, arXiv e-prints, arXiv:2202.13859
Khotanzad, A. & Hong, Y. H. 1990, IEEE Transactions on pattern analysis and machine intelligence, 12, 489
Klimchuk, J. A., van Driel-Gesztelyi, L., Schrijver, C. J., et al. 2009, Transactions of the International Astronomical Union, Series A, 4, 79
Krucker, S. & Benz, A. O. 1998, ApJ, 501, L213
Lemen, J. R., Title, A. M., Akin, D. J., et al. 2012, Sol. Phys., 275, 17
Lin, R. P., Schwartz, R. A., Kane, S. R., Pelling, R. M., & Hurley, K. C. 1984, ApJ, 283, 421
Lu, E. T., Hamilton, R. J., McTiernan, J. M., & Bromund, K. R. 1993, ApJ, 412, 841
Madjarska, M. S. 2019, Living Reviews in Solar Physics, 16, 2
Mandal, S., Peter, H., Chitta, L. P., et al. 2021, A&A, 656, L16
Mason, J. P. & Hoeksema, J. T. 2010, ApJ, 723, 634
Mayo, D. G. & Cox, D. R. 2006, in Optimality (Institute of Mathematical Statistics), 77–97
McAteer, R. T. J., Aschwanden, M. J., Dimitropoulou, M., et al. 2016, Space Sci. Rev., 198, 217
Müller, D., St. Cyr, O. C., Zouganelis, I., et al. 2020, A&A, 642, A1
Noori, M., Javaherian, M., Safari, H., & Nadjari, H. 2019, Advances in Space Research, 64, 504
Panesar, N. K., Tiwari, S. K., Berghmans, D., et al. 2021, ApJ, 921, L20
Parenti, S., Buchlin, E., Cargill, P. J., Galtier, S., & Vial, J. C. 2006, ApJ, 651, 1219
Parker, E. N. 1988, ApJ, 330, 474
Parnell, C. E. 2002, in Multi-Wavelength Observations of Coronal Structure and Dynamics, ed. P. C. H. Martens & D. Cauffman, Vol. 10, 47
Parnell, C. E. & Jupp, P. E. 2000, ApJ, 529, 554

Pauluhn, A. & Solanki, S. K. 2007a, A&A, 462, 311
Pauluhn, A. & Solanki, S. K. 2007b, A&A, 462, 311
Porter, J. G. & Dere, K. P. 1991, ApJ, 370, 775
Potts, H. E., Barrett, R. K., & Diver, D. A. 2004, A&A, 424, 253
Powers, D. M. W. 2011, Machine Learning Technologies, 2, 37
Priest, E. 2014, Magnetohydrodynamics of the Sun (Cambridge University Press)
Raboonik, A., Safari, H., Alipour, N., & Wheatland, M. S. 2017, ApJ, 834, 11
Reale, F. 2014, Living Reviews in Solar Physics, 11, 4
Rochus, P., Auchère, F., Berghmans, D., et al. 2020, A&A, 642, A8
Shokri, Z., Alipour, N., Safari, H., et al. 2022, ApJ, 926, 42
Strugarek, A. & Charbonneau, P. 2014, Sol. Phys., 289, 4137
Tajfirouze, E. & Safari, H. 2012, ApJ, 744, 113
Teriaca, L., Banerjee, D., Falchi, A., Doyle, J. G., & Madjarska, M. S. 2004, A&A, 427, 1065
Tiwari, S. K., Panesar, N. K., Moore, R. L., et al. 2019, ApJ, 887, 56
Upendran, V. & Tripathi, D. 2021, ApJ, 916, 59
Vaiana, G. S., Davis, J. M., Giacconi, R., et al. 1973a, ApJ, 185, L47
Vaiana, G. S., Krieger, A. S., & Timothy, A. F. 1973b, Sol. Phys., 32, 81
van Ballegooijen, A. A. & Martens, P. C. H. 1989, ApJ, 343, 971
Verbeeck, C., Kraaikamp, E., Ryan, D. F., & Podladchikova, O. 2019, ApJ, 884, 50
Veronig, A., Temmer, M., Hanslmeier, A., Otruba, W., & Messerotti, M. 2002, A&A, 382, 1070
Vlahos, L., Georgoulis, M., Kluiving, R., & Paschos, P. 1995, A&A, 299, 897
Yousefzadeh, M., Safari, H., Attie, R., & Alipour, N. 2016, Sol. Phys., 291, 29
Zhukov, A. N., Mierla, M., Auchère, F., et al. 2021, A&A, 656, A35

[1] Department of Physics, Faculty of Science, University of Zanjan, : University Blvd., Zanjan, 45371-38791, Zanjan, Iran
[2] Observatory, Faculty of Science, University of Zanjan, : University Blvd., Zanjan, 45371-38791, Zanjan, Iran
[3] Solar-Terrestrial Centre of Excellence – SIDC, Royal Observatory of Belgium, Ringlaan -3- Av. Circulaire, 1180 Brussels, Belgium
[4] Université Paris-Saclay, CNRS, Institut d'Astrophysique Spatiale, 91405 Orsay, France
[5] Max Planck Institute for Solar System Research, Justus-von-Liebig-Weg 3, 37077 Göttingen, Germany
[6] Department of Mathematics, Physics and Electrical Engineering, Northumbria University, Newcastle Upon Tyne, NE1 8ST, United Kingdom
[7] ETH-Zürich, Hönggerberg campus, HIT building, Zürich, Switzerland
[8] Physikalisch-Meteorologisches Observatorium Davos,World Radiation Center, 7260, Davos Dorf, Switzerland
[9] RCAAM of the Academy of Athens, 4 Soranou Efesiou Street, 11527 Athens, Greece
[10] UCL-Mullard Space Science Laboratory, Holmbury St. Mary, Dorking, Surrey, RH5 6NT, UK
[11] Leibniz Institute for Astrophysics in Potsdam (AIP), An der Sternwarte 16, 14482 Potsdam, Germany
[12] Centre for mathematical Plasma Astrophysics, Mathematics Department, KU Leuven, Celestijnenlaan 200B bus 2400, B-3001 Leuven, Belgium
[13] Southwest Research Institute, 1050 Walnut Street, Suite 300, Boulder, CO 80302, USA
[14] Skobeltsyn Institute of Nuclear Physics, Moscow State University, 119992 Moscow, Russia